Temperature dependent second-order Raman scattering in CuI

R. Hildebrandt,[1,*] M. Seifert,[2] J. George,[3,2] S. Blaurock,[4] S. Botti,[2] H. Krautscheid,[4] M. Grundmann,[1] and C. Sturm[1]

[1] *Universität Leipzig, Felix Bloch Institute for Solid State Physics, Semiconductor Physics Group, Linnéstraße 5, 04103 Leipzig*

[2] *Friedrich-Schiller-Universität Jena, Institute of Condensed Matter Theory and Optics, Max-Wien-Platz 1, 07743 Jena*

[3] *Federal Institute for Materials Research and Testing Department Materials Chemistry, Unter den Eichen 87, 12205 Berlin*

[4] *Univerität Leipzig, Institute for Inorganic Chemistry, Johannisallee 29, 04103 Leipzig*

(Dated: May 25, 2023)

We report second-order Raman scattering spectra of copper iodide bulk single crystals aside from the fundamental TO and LO mode. The spectral shape was reproduced by a 2-phonon density of states calculated by DFT. Characteristic multi-phonon features were identified and assigned to combination, overtone and difference modes. In this way, the energy of acoustic zone-boundary phonons was determined. The temperature dependence of those modes and the fundamental optical phonons was analyzed by means of phonon-phonon interactions and lattice expansion effects up to room temperature. Processes related to the mode energy shift and width were identified for phonons at high symmetry points. The shifts due to lattice expansion are in accordance with the predictions by DFT in quasi-harmonic approximation using PBEsol functional.

I. INTRODUCTION

Wide-bandgap semiconductors like ZnO, GaN or SiC are nowadays established for high power or high frequency applications, while sadly their intrinsic n-type charge carriers sets limitations [1]. For these materials, the intrinsic p-type semiconductor copper iodide (CuI) [2] represents a possible complement due to its large bandgap of 3.1 eV with hole mobility of up to 43 cm^2/Vs [3]. Its crystal structure at room temperature (RT) is zincblende. A large exciton binding energy of about 62 meV is promising for opto-electronic applications as well its high thermoelectric figures of merit [4]. Device applications in hetero pn-junctions were demonstrated for solar cells [5], transistors [6] and light emitting diodes [7].

The interest in CuI is continued by recent investigations of various growth techniques using the temperature difference method [8] for bulk crystals, pulsed laser deposition [9] or solution based methods [10] for thin films or micro wires by vapor-phase transport [11]. In this way, usually (111)-oriented films or crystal facets are obtained. By molecular beam epitaxy the growth of (110)- and (001)-oriented films was demonstrated as well [12]. Depending on the deposition technique and parameters, p-type charge carrier concentrations in a range of 4×10^{16}cm^{-3} up to 1×10^{20}cm^{-3} were achieved [3, 4, 9].

Remarkable for CuI is the large exciton oscillator strength, which is larger than for GaN and comparable to ZnO, leading to the formation of exciton-polaritons [13–15]. Sub-bandgap emission properties gave indication for the Cu vacancy as a relevant intrinsic material defect [16, 17]. This is also supported by a stabilizing effect, predicted by calculations [18]. Effects on the band structure due to doping or temperature were also investigated in detail [19, 20]. Via neutron scattering [21], infrared transmission [22] as well as Raman spectroscopy, the phononic properties of CuI were analyzed [23–28].

While for fundamental TO and LO phonons the pressure and temperature dependence were investigated quite well, the weaker second-order Raman scattering signals were reported only once up to now [29]. Second-order Raman spectra can be used to collect information on the overall phonon dispersion, especially for acoustic phonons at high symmetry points. This is relevant for thermal transport properties [30], in nanostructures or electron-phonon coupling [31], phonon reabsorption [32] or non-radiative recombination [33] processes.

Here we report on the fundamental phonon properties of CuI, which are determined with high precision and resolution at high symmetry points. We investigate the temperature behavior as well and discuss harmonic and anharmonic contributions to the phonon properties. The paper is structured as follows: Relevant experimental and computational methods are described in Section. II. In Sec. III we present and discuss the assignment of CuI's second-order Raman features, their temperature dependence, the harmonic and anharmonic contributions for the fundamental TO and LO modes which builds the basis for using a Klemens-like Model [34] to analyze the acoustic phonons at high symmetry points. The results are summarized in Sec. IV.

II. METHODS

A. Crystal growth and quality

By using copper acetate monophydrate (Sigma-Aldrich, 98%), acetone and iodine (Sigma-Aldrich, 99.5%), copper iodide was synthesized in hot acetic acid. The procedure was similar to the one reported by Hardt and Bollig [35]. The purification of the crude product, was carried out by crystallization, followed by thermal decomposition of an acetonitrile copper iodide complex $[(CH_3CN)_2(CuI)_2]_n$ [15]. The crystal growth of copper iodide single crystals was realized in autoclaves by taking advantage of the inverse temperature-dependent solubility of copper iodide in acetonitrile [36], similar to the procedure of Krüger *et al.* [15]. The resulting γ-CuI bulk crystals were colorless with typical dimensions in

* ron.hildebrandt@uni-leipzig.de

the range of 1-4 mm.

The purity of the crystals was determined to be larger than 99.999% with a Bruker S2 Picofox TXRF using a multi-element standard.

Structural characterization of the crystals was done by X-ray diffraction using a PANalytical X'Pert Pro diffractometer with a Cu K_α. The crystal facets were (111)-oriented and a cubic lattice constant of a =6.053(3) Å was determined. ϕ-scans of asymmetrical reflections indicated no twinning or rotational domains of the crystals. Details of the procedures and X-ray diffraction scans can be found in Ref. 15.

B. Raman scattering

All Raman measurements were performed in a helium flow cryostate (Janis ST-500) with the CuI single crystal fixed on a c-plane sapphire substrate. The temperature was determined by using a calibrated silicon diode mounted on the cold finger. As excitation source we used a 100 mW diode pumped solid-state laser ($\lambda = 532.06$ nm, Coherent Compass 315M). A microscope objective with an $NA = 0.42$ (Mitutoyo) was used in a back scattering configuration and a Glan-Thompson prism and a half-wave plate was used to analyze the linear polarization. A double monochromator (Jobin Yvon U1000) with a focal length of 2×1m and a 2400 lines/mm grating resulted in a spectral resolution of about 0.2 cm^{-1} (CCD: Symphony II BIUV). One measurement window spanned over about 115 cm^{-1}, with about 17% spectral overlap of two distinct measurements. Rotational Raman lines of air were observed (removed later from spectra) and used for calibration of Raman shift features up to 150 cm^{-1}.

C. Computational details

The computations were done in the framework of density functional theory (DFT) using the Vienna *ab initio* simulation package VASP [37, 38] with the projector-augmented wave method [39]. The 4*s* and 3*p* electrons of Cu and 5*s* and 5*p* electrons of I are thereby treated explicitely as valence electrons. Starting with the pure zincblende γ-phase, we used a cutoff energy of 770 eV for the plane-wave basis set and **k**-point grid of 8×8×8. We used here tighter computational settings than in our other studies on CuI [40, 41], to avoid spurious imaginary modes around Γ-point as a potential result of numerical noise [42]. We have applied the exchange-correlation functional PBEsol [43] for structural optimizations and phonon computations. For the full structural optimization with DFT at 0 K, we relaxed all forces until they were smaller than 10^{-5} eV/Å. This led to a lattice parameter of 5.940 Å for PBEsol which is quite close to the experimental value of 6.053 Å. For the calculation of the Born charges for the non-analytical corrections (NAC), we used a denser **k**-point grid of 16×16×16.

For the phonon calculations, we used the package phonopy [44, 45] together with VASP and computed the harmonic phonons with the help of the the finite displacement method with a displacement of 0.01 Å. We used 4×4×4 supercells of the primitive cell with a **k**-point grid of 2×2×2 for the computation of the forces. Information on the convergence of the supercell size are given in the supporting information. For the calculation of the 1-Phonon density of states (1PDOS) and the thermal properties, we used a **q**-point mesh of 16×16×16. For the broadening of the 1PDOS, we use a gaussian smearing with a full width half maximum (FWHM) of 2 cm^{-1}. To compute the temperature-dependence of the phonon modes, we relied on the quasi-harmonic approximation [46]. For this we chose different volumes roughly around ± 10% of the DFT minimum volume. All these cells were relaxed with the constraint to keep the volume constant. We then performed phonon calculations with consistent settings, mentioned above, for these different volumes around the DFT minimum volume to obtain a description of the free energy as a function of volume at different temperatures. Based on this, we obtain the temperature-dependent equilibrium volumes and repeated the phonon calculations at those volumes corresponding to certain temperatures. More details regarding this procedure are shown in the supplementary.

The 2-phonon density of states (2PDOS) was obtained out of the phonon frequencies following the equation as defined by Ref. [47]:

$$\begin{aligned} \mathrm{2PDOS}(\vec{q}, j) = 2\pi \sum_{\vec{q}',\vec{q}''} \sum_{j',j''} \Delta\left(\vec{q} - \vec{q}' - \vec{q}''\right) \\ \times \delta\left(\omega(\vec{q}, j) - \omega\left(\vec{q}', j'\right) - \omega\left(\vec{q}'', j''\right)\right) \end{aligned} \quad (1)$$

$\Delta(\vec{Q})$ is 1, if $\vec{Q}$ is either zero or a reciprocal lattice vector. Otherwise the $\Delta(\vec{Q})$ is zero. Furthermore $\vec{q}$ denotes the phonon wave vector, j the corresponding phonon mode and ω the phonon frequency. While determining the 1PDOS we obtain the phonon modes at each sample point in the Brillouin zone and therefore attain all information needed to calculate the 2PDOS via Eq. (1). The 2PDOS was broaded with a Gaussian smearing, with a full width half maximum (FWHM) of 2 cm^{-1}.

III. RESULTS AND DISCUSSION

A. Second-order Raman features

The millimeter-sized single crystals were cooled down to about 10 K and Raman spectra with different integration time in parallel- (z(xx)$\bar{\mathrm{z}}$) and cross-polarization (z(xy)$\bar{\mathrm{z}}$) were measured to observe the first- and second-order Raman scattering features of CuI.

The first-order spectra can be seen in Fig. 1(a) and show the transversal optical (TO) and longitudinal optical (LO) mode at 133.3 cm^{-1} and 149.4 cm^{-1} respectively. The second-order Raman signal is shown as well and multiplied by a factor of 300 for clarity. This signal contains four large structures labeled A, B, C and D with various features which are listed in detail in Tab. I. From the phonon dispersion in Ref. 21, each structure's origin can be estimated by using the CuI phonon dispersion.

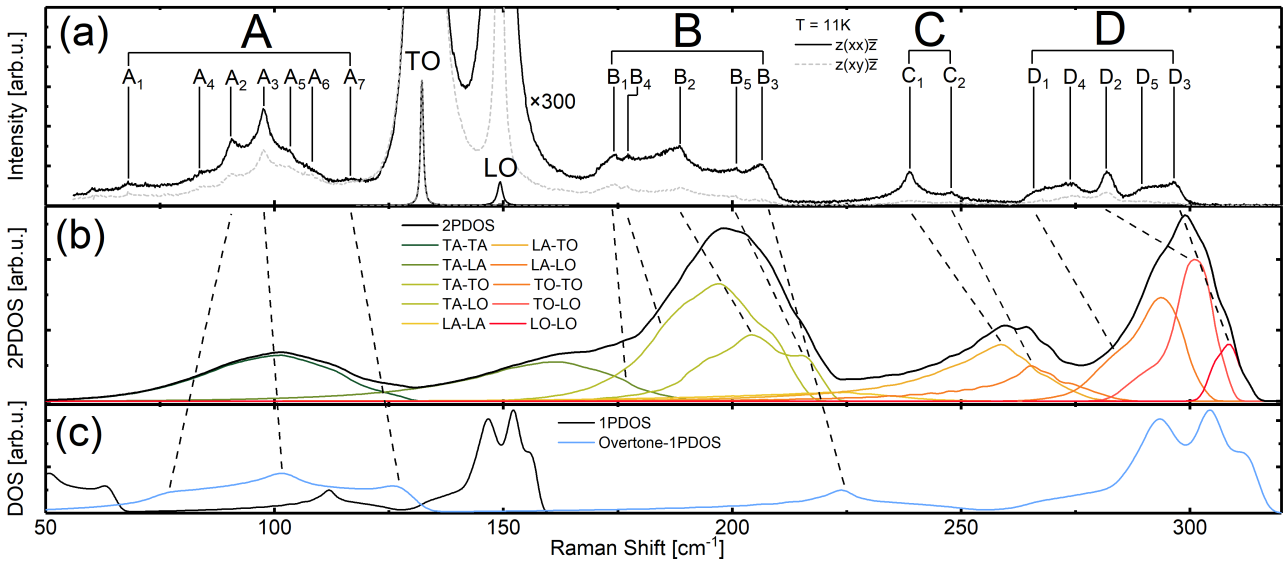

FIG. 1. (a) Second-order Raman spectrum of CuI at 11 K for parallel (black, z(xx)$\bar{z}$) and cross (grey, z(xy)$\bar{z}$) polarization. The TO and LO mode are represented by the signal which is 300 times weaker, as well in both polarizations. Four large structures A, B, C and D are observed whereby each fine feature is labeled and listed with details in Tab. I. (b) 2-phonon DOS calculated via the PBEsol phonon dispersion. (c) PBEsol 1-phonon DOS (1PDOS) and Overtone-1PDOS. The higher energy of calculated features compared to the observed experimental ones is related to larger optical phonon energies predicted by PBEsol.

In a second-order Raman process, two phonons are involved in the scattering process. There are three different processes relevant to identify the feature's origin: overtone-, combination- and difference-phonon modes. The overtone process is characterized by a contribution of two phonons from the same phonon branch, with opposite momenta. If their wavenumber is, for example, ω_a, the resulting observed Raman shift is at $2\omega_a$. The phonon combination $(+)$ or difference $(-)$ processes are characterized by two phonons of different phonon branches whereby both phonons have opposite momenta. If their wavenumbers, for example, are ω_a and ω_b, the resulting observed Raman shift is at $\omega_a \pm \omega_b$. Momentum conservation is ensured in each processes via opposite momenta of the respective contributing phonons ($q \approx 0$).

We now proceed with discussing our assignment of the observed structures, based on CuI's known phonon dispersion [21]. The observed structure between 75 cm^{-1} and 120 cm^{-1} (labeled A) were attributed to overtones of transversal acoustic (TA) phonons, whereas the structure between 270 cm^{-1} and 300 cm^{-1} (labeled D) are attributed to combinations and overtones of optical phonons. The intermediate structures labeled B ($170-210\,\mathrm{cm}^{-1}$) and C ($235-250\,\mathrm{cm}^{-1}$) can be attributed to combinations and overtones of optical and acoustic phonons. For the structure B, mostly TA and optical phonons are involved, while for the structure C, LA and optical phonons participate. Between each structure, a featureless continuum signal is observed. Each feature is here associated with van Hove singularities of the 2PDOS.

The selection rules for second-order Raman processes in zincblende crystals yield that all combinations and overtones are allowed [48] and hence the information of the full phonon dispersion is contained in the second-order Raman spectrum [49–51].

To refine the assignment, we will also include estimates of the intensities from the computed phonon dispersion. The intensity dependence of the individual second-order Raman features is quite complex. It depends upon the phonon dispersion, the second-order Raman susceptibilities of the phonon branches as well as their population. Usually, the spectral shape can be approximated by using the overtone phonon density of states (Overtone-1PDOS), which is the phonon density of states (1PDOS) multiplied by a factor of 2 [49]. This especially emphasizes overtone processes, whereby combination processes are only represented in the 2-phonon DOS (2PDOS, calculated via Eq. 1). The 2PDOS and the Overtone-1PDOS are shown in Fig. 1(b, c). Considering both contributions, the origin of each feature can be assigned and in this way, the individual phonon energies can be derived.

For all observed features, the involved phonons as well as their energy and the corresponding wave vector in the BZ are summarized in Tab. II. For TA phonons, the L and X critical points are easily observable, while for the LA phonons the high density of states favors the observation of $\mathrm{LA_L}$ related overtones and combinations. Hence, the $\mathrm{LA_X}$ mode can be neglected in most cases, because of its low density of states. This is similar to ZnS, which has a quite comparable phonon dispersion compared to CuI [52, 53] due to the relative atomic masses and their high transversal charge values [54]. The $\mathrm{LA_L}$ DOS dominance is as well indicated by the phonon dispersion in Ref. [55]. This is also supported by a strong parallel-polarized signal at the $\mathrm{B_3}$ feature, which can be characteristic for overtones [49]. Due to the low dispersion of the optical phonons, all their combinations and overtones are clearly observed as well. In this way, most features were uniquely iden-

tified, while only three features are ambiguous.

Deviations from the observed peak position and the phonon energy at the critical point can be seen for example clearly at the D_3 feature. This feature D_3 (297 cm^{-1}) shows a deviation to its LO_Γ overtone assignment (298.6 cm^{-1}) by 1.6 cm^{-1}. Deviations of similar magnitude can be observed for other assignments and are usually lower than 2 cm^{-1}. Those deviations can be explained by the different type of maxima involved in the respective 2-phonon scattering transitions and the flatness of the phonon dispersion at respective brillouin zone points. This would reason a deviation of the 2-phonon density of states maximum [56], compared to the position from the critical points of the phonon dispersion.

From the observed second-order Raman features, the phonon energies at certain critical points in the BZ were deduced and were given in Tab. II. We observed a good agreement with those determined by neutron scattering [21, 55]. For acoustic phonons, only the TA phonon at the L-point were observed a higher wavenumber. The energetic ordering of the optical phonons at the respective critical points is resembled in addition to assuming a non-crossing behavior of the TO and LO mode, as in the phonon observed for the phonon dispersions in Ref. [55]. This is expected for CuI due to its high transversal charge similar to ZnS [22, 23, 53, 57, 58]. The non-crossing, though, is not reproduced by our calculated phonon dispersion. Similar deviations between experimental and calculated phonon dispersion are as well observed for CuBr or ZnTe [53, 55, 59]. Nevertheless, the spectral shape is well resembled by the 2PDOS.

For the optical overtones (structure D), the present crossing of TO and LO phonon in the DFT-based phonon dispersion reasons a weak separation of individual TO-TO (D_1), TO-LO (D_2) and LO-LO (D_3) phonon combinations. This is better represented by the Overtone-1PDOS or through the individual parts of the 2PDOS, but not by the full 2PDOS (Fig. 1(b, c)).

TABLE I. Labels and position of observed Raman features. Assignments of involved phonons are done with the position in the brillouin zone by critical point labels. Along the Σ-direction, these additional energies were assumed: $LA_\Sigma = (LA_X + LA_L)/2 = 114 cm^{-1}$, $TA_{\Sigma,l} = (TA_X + TA_L)/2 = 47 cm^{-1}$, $TA_{\Sigma,u} = 61 cm^{-1}$ and $LO_\Sigma = LO_X$. The indices "l" and "u" indicate the lower and upper TA phonon branch along the Σ direction. The last column contains the second-order phonon feature energy predicted by our suggested critical point phonon energies from Tab. II. All energies are given in cm^{-1}.

Label	Experiment [cm^{-1}]	Prediction via Tab. II [cm^{-1}]	Assignment	Point
A_1	67.5[a]	67	LA - TA_l	Σ
A_4	84[a]	83	LO - TA_u	Σ
A_2	90.5	90	2TA	L
A_3	97.5	98	2TA	X
A_5	103	-	2TA	K?
A_6	108	-	2TA	W?
A_7	>116	122	$2TA_u$	Σ
B_1	173.5[a]	173	TA + LA	X
		175	TA_u + LA	Σ
B_4	177	181	TA + TO	L
B_2	188.5	≈190	TA + TO	X
		≈193	TA + LO	X
		190	TA + LO	L
B_5	200.5	≈ 200	TA_u + O	Σ
B_3	206	206	2LA	L
C_1	238.5	238	LA + TO	L
C_2	247.5	248	LA + LO	L
D_1	265.5	264.4	2TO	Γ
D_4	274	270	2TO	L
D_2	282	280, 285, 281.5	TO + LO	L,X,Γ
		282	2TO	X
D_5	291	290, 288	2LO	L,X
D_3	297	298.6	2LO	Γ

[a] Also observed in Ref. 29.

B. Temperature dependence of Raman modes

The identified features in the second-order Raman spectrum at low temperature were related to the combinations, differences and overtones of various acoustic and optical phonon modes. With increasing temperature a Raman shift to lower wavenumbers of the features is observed in addition to a strong linewidth increase. This restricts the number of traceable features at elevated temperatures. The measured Raman spectra as a function of temperature are shown in Fig. 2.

The intensity of the structures B, C and D rises with increasing temperature according to $I_{sum} \propto [n(\omega_a)+1][n(\omega_b)+1]$, as expected for overtone and combinations modes [25, 60]. Here $n(\omega_i) = [\exp(hc\omega_i/k_B T)-1]^{-1}$ is the Bose-Einstein distribution function with ω_i the wavenumber of the phonon. For the structure A, an additional contribution from a difference mode has to be considered, i.e. $I_A \propto I_{sum} + [n(\omega_c)+1][n(\omega_d)]$ with $\omega_c - \omega_d \approx 90\,cm^{-1}$. This difference mode contribution vanishes for low temperatures and can be neglected at 10 K. At room temperature (RT), this mode, labeled here A-DM (difference mode), is easily observable at about 90 cm^{-1} [23]. Its intensity is then comparable to the TO and LO mode and its origin involves various optical and TA phonons.

Due to the strong linewidth broadening, most features are only observable up to about 100 K or 200 K, respectively. The energy as a function of temperature is shown for all respective features in Fig. 3.

We assign the features A_1 and A_4 as difference modes. This assignment was supported by the observed temperature dependencies of their intensities [25, 60]. The structure D shifts twice as fast as the fundamental TO and LO modes, as expected for overtone and combination modes.

With the known origin of the features (Tab. I) and their temperature dependence, the temperature dependence of acoustic phonons can be determined, which are otherwise not accessible via first-order Raman scattering. The energy of the TA phonons at the L- and X-point is given by their overtones represented by feature A_2 and A_3 respectively. The LA_X phonon can be related to B_1 - $A_3/2$ while LA_L is related to $B_3/2$.

Before the acoustic phonons' temperature dependence is

TABLE II. Phonon mode energies at critical points Γ, L and X determined from the second-order Raman scattering spectrum at 9 K. In parentheses are the respective energies determined via neutron scattering at RT from Ref. 21. Their error, derived from CuBr measurement, is about $\pm 5\,\mathrm{cm}^{-1}$. The last columns are our estimated uncertainties of the respective energies considering measurement inaccuracies and deviations resulting from the 2PDOS shape. All values are given in cm^{-1}.

Mode	ω_Γ	ω_L	ω_X	$\Delta\omega_\Gamma$	$\Delta\omega_L$	$\Delta\omega_X$
TA	-	45.3 (34)	49.3 (43)	-	0.3	0.3
LA	-	103 (102)	124 (118)	-	2	2
TO	132.2 (128)	135 (134)	141 (143)	0.1	2	4
LO	149.3 (163)	145 (157)	144 (157)	0.1	2	4

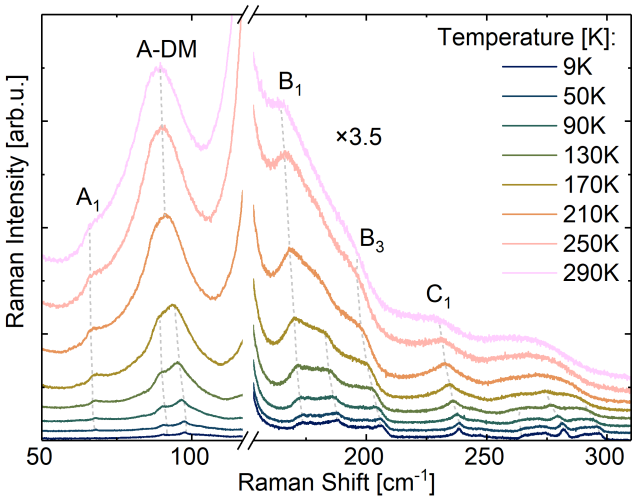

FIG. 2. Temperature-dependent unpolarized second-order Raman spectra of CuI up to room temperature in 40 K steps. The intensity of the features above the horizontal break are scaled up by 3.5 for better visibility. Some prominent features at different temperatures are indicated by grey dashed lines and/or labels.

derived, the impact of the lattice expansion and the phonon-phonon interaction on the properties of the optical phonons at the Γ-point is discussed. This will later support the validity of derived anharmonic contributions, observed in the shifts of acoustic phonons.

C. Optical phonons

The fundamental TO and LO phonons at the Γ-point were analyzed by means of Lorentzian functions regarding their width and position. This data is shown in Fig. 4. The data can be described by the Klemens-like model, in which the Raman shift and the mode width are related to harmonic effects of the crystal lattice and anharmonic phonon-phonon interactions, i.e. one phonon decays into multiple other phonons [34, 61, 62]. Both contributions can be described by the complex energy, whereby the real part describes the mode's renormalization of frequency and the imaginary part is related to the lifetime of the phonon, i.e., its linewidth.

Considering contributions from the lattice expansion and the decay of phonons into up to three phonons, the Raman shift of the phonon mode as a function of temperature can be described by [24, 61, 62]:

$$\omega(T) = \omega_0 - \Delta_{\mathrm{Lat.}}(T) + \Delta_{\mathrm{3ph}}(T) + \Delta_{\mathrm{4ph}}(T) \tag{2}$$

where ω_0 is the unperturbed phonon energy, Δ_{3ph}, Δ_{4ph} are the anharmonic phonon decay processes involving 3 or 4 phonons respectively and $\Delta_{\mathrm{Lat.}}$ is the Raman shift of the phonon due to thermal expansion of the crystal lattice, which is given in detail by [24, 61]:

$$\Delta_{\mathrm{Lat.}}(T) = 3\omega_0\gamma\int_0^T \alpha(T')\,\mathrm{d}T'. \tag{3}$$

Here γ denotes the Grüneisen parameter and α the temperature dependent coefficient of the thermal expansion. The temperature dependence of the thermal expansion coefficient was taken from Ref. 12 (see supplementary).

The contributions of the anharmonic processes are described by [34, 62]:

$$\begin{aligned}\Delta_{\mathrm{3ph}}(T) &= \Delta_3[1+\textstyle\sum_{i=1}^{2} n(\omega_i)]\\ \Delta_{\mathrm{4ph}}(T) &= \Delta_4[1+\textstyle\sum_{j=1}^{3} n(\omega_j)+n^2(\omega_j)]\end{aligned} \tag{4}$$

with Δ_3 and Δ_4 as zero temperature renormalization constants describing the strength of the individual contributions to the Raman shift. Energy conservation has to be satisfied by $\omega_0 = \sum_{i=1}^{2}\omega_i = \sum_{j=1}^{3}\omega_j$.

For the broadening, the impact of the crystal lattice can be neglected, i.e., the broadening is determined by the anharmonic phonon-phonon interaction and by defects and is given by:

$$\begin{aligned}&\Gamma(T) = \Gamma_{\mathrm{3ph}}(T) + \Gamma_{\mathrm{4ph}}(T) + \Gamma_{\mathrm{Defect}},\\ &\quad\text{with}\\ &\Gamma_{\mathrm{3ph}}(T) = \Gamma_3\cdot[1+\textstyle\sum_{i=1}^{2} n(\omega_i)]\\ &\Gamma_{\mathrm{4ph}}(T) = \Gamma_4\cdot[1+\textstyle\sum_{j=1}^{3} n(\omega_j)+n^2(\omega_j)]\end{aligned} \tag{5}$$

Here Γ_3 and Γ_4 are again constant parameters related to their type of contribution respectively. Γ_{Defect} accounts for defect contributions and was set to 0, due to the high sample quality indicated by X-ray fluorescence and X-ray diffraction measurements.

The Grüneisen parameters γ of the respective phonon modes were taken from Ref. 23 with $\gamma(\mathrm{TO}_\Gamma) = 1.8$ and $\gamma(\mathrm{LO}_\Gamma) = 2.5$. This is in accordance with other results [63, 64]. Our calculated Grüneisen parameter band structure is shown in the supplementary.

By a line-shape analysis by means of Lorentzian functions, the mode properties (broadening and energy) of the first-order TO and LO modes were determined. The data is shown in Fig. 4 (open squares). The model to describe these changes of the optical phonons is fitted to the experimental data (black line). The individual contributions from the lattice expansion

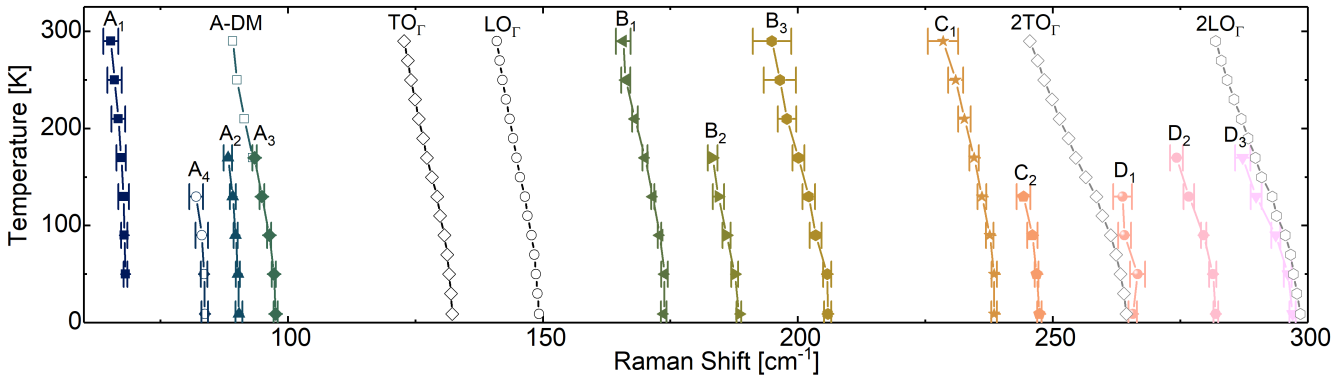

FIG. 3. Temperature dependence of second-order Raman scattering features and the fundamental TO and LO mode including their expected overtone positions. The A-DM mode (not listed in Tab. I) is related to various difference processes and has comparable intensity at RT as the fundamental modes.

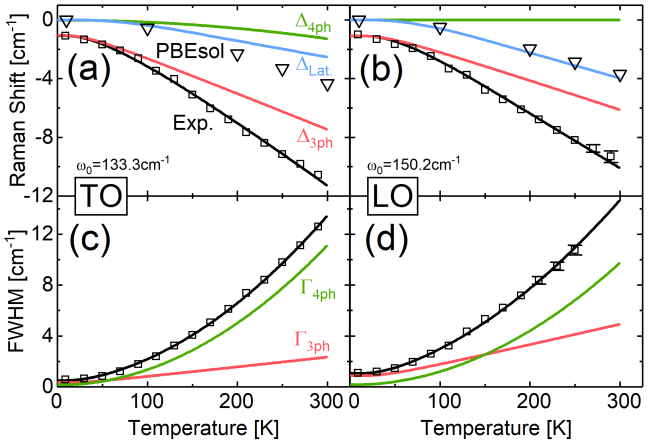

FIG. 4. Experimental Raman shift for the TO (a) and LO (b) mode as well as the FWHM for the TO (c) and LO (d) mode in dependence of the temperature (open squares). A model fit (black) with the individual contributions of the 3-phonon process Δ_3 (red), 4-phonon process Δ_4 (green) and the lattice $\Delta_{\mathrm{Lat.}}$ (light blue) describes the observations. The quasi-harmonic Raman shifts are predicted by PBEsol (black open triangles). ω_0 is the unperturbed phonon energy. Error bars not indicated are smaller than the symbol size.

TABLE III. Fit parameters obtained via Eq. 2 and 5. The fits are shown in Fig. 4 and Fig. 5. For these parameters, Klemens-like recombination channels were always assumed ($\omega_i \approx \omega_0/2$). Errors are indicated below respective values. All quantities are given in cm^{-1}.

Mode	ω_0	ω_i	ω_j	Δ_3	Δ_4	Γ_3	Γ_4
TO_Γ	133.3	67	45	-1.26	-0.013	0.36	0.17
	±0.1			±0.1	±0.01	±0.06	±0.01
LO_Γ	150.2	75	50	-1.1	0	0.9	0.18
	±0.2			±0.2	±0.02	±0.15	±0.02

(light blue), 3-phonon (red) and 4-phonon (green) processes are as well shown as solid lines. The quasi-harmonic Raman shift predicted by PBEsol (black open triangles) calculations are indicated. The LO FWHM at 270 K and above was excluded from the fit due to a strong influence of the second-order Raman signal and overlap with the TO peak.

The model fits nicely the experimental data for the Raman shifts as well for the line widths. The general behavior is quite similar for the TO and LO mode.

For both modes, the Raman shifts are dominated by the 3-phonon process, including a weaker lattice contribution. This lattice contribution matches quite exactly the PBEsol calculations for the LO mode (black triangles), while for the TO mode a deviation is observed. Nevertheless, the trend is well resembled. A weak contribution of the 4-phonon process is found for the TO mode only and completely absent for the LO mode.

The fit parameters describing the Raman shift of the TO and LO mode in Tab. III are in agreement with the earlier results from Ref. 23 (under consideration of isotope effect). The ratio $\Delta_{3,\mathrm{TO}} / \Delta_{3,\mathrm{LO}} \approx 1$ is similar to the one reported in Ref. [23]. Our result of $\Delta_4 \approx 0$ supports their approach to neglect 4-phonon processes. The difference in absolute values can be explained by the fact that a contribution due to the lattice expansion, which enforces larger Δ_3 values, was not included in Ref. [23].

The results dependence on the choice of the ω_i or ω_j parameters is negligibly weak. Hence one can not exclude the presence of multiple decay channels, which have comparable ω_i values. For example $\mathrm{LO}(150\,\mathrm{cm}^{-1}) \rightarrow \mathrm{LA}(100\,\mathrm{cm}^{-1}) + \mathrm{TA}(50\,\mathrm{cm}^{-1})$ is expected to be present in similar magnitude as $\mathrm{LO}(150\,\mathrm{cm}^{-1}) \rightarrow \mathrm{LA}(75\,\mathrm{cm}^{-1}) + \mathrm{LA}(75\,\mathrm{cm}^{-1})$. Only for extreme cases a differentiation is possible. These would require the observation of a stronger pronounced kink in the Raman shift. In this way, a significant contribution of energetically strongly asymmetric decay channels can be excluded such as, for example, found for the $\mathrm{LO}(150\,\mathrm{cm}^{-1}) \rightarrow \mathrm{TO}(132\,\mathrm{cm}^{-1}) + \mathrm{TA}(18\,\mathrm{cm}^{-1})$ channel.

The PBEsol results for the mode shift as a function of temperature of the TO and LO modes are much lower than the experimentally observed shift of the phonon modes. However, their contribution is approximately equal to the lattice contribution, which was calculated by the individual Grüneisen parameters (from Ref. [23], derived via linear response method within DFT) and the experimental coefficient of thermal ex-

pansion (from Ref. [12]). We use a quasi-harmonic model which only accounts for volume expansion to compute the frequency shift. Therefore, it is not surprising at all, that we only capture this effect. Hence, the PBEsol results can be associated with the lattice expansion contribution.

The line widths of the TO and LO modes behave as well quite similar. The 4-phonon process dominates the linewidth increase at large temperatures while, at low temperatures, the 3-phonon process is dominant. This is especially the case for the LO mode, which results in the larger zero-temperature linewidth of 1.03 cm^{-1} compared to 0.53 cm^{-1} for the TO mode. These values agree well with the ones reported in Ref. 23. At elevated temperatures, the TO and LO width characteristics are reproduced [23, 24] (considering the copper isotope distribution).

Overall, the 3- and 4-phonon processes are relevant for both the renormalization and the width of the respective phonon modes as well as the lattice expansion contribution for the renormalization. The anharmonic effects dominate CuI's characteristics, especially compared to other materials. This could be linked to metastable dynamics of intrinsic defects [65]. Nevertheless, the observed behavior is well explained by the Klemens model [34] for both optical phonons and the results are in accordance with other publications [23, 24]. The strong anharmonicity effects observed here for CuI could possibly be linked to meta stable dynamics of intrinsic defects [65].

D. Acoustic phonons

The experimentally determined TA_L, TA_X, LA_L and LA_X phonon energies at the respective temperature are shown in Fig. 5(a-d). The experimental data for the LA_L mode shows a linear dependence, in agreement with results from Refs. [66–68]. The shift of the acoustic phonons from 10 K up to RT is in the range of 2-6 cm^{-1} and is significant smaller compared to the shifts of the optical ones.

The model by Klemens is only valid for zone-center optical phonons [34]. The observed shifts of the acoustic TA and LA phonons at the L and X point look in principle similar to the ones observed for the TO and LO phonons. Hence, we adapt this for a phenomenological description by including the known lattice expansion and Grüneisen parameters for the respective phonons at the critical points [23] ($\gamma(TA_L) = -0.9$, $\gamma(TA_X) = -0.3$, $\gamma(LA_L) = 1.5$ and $\gamma(LA_X) = 2.2$). An influence due to the choice of Grüneisen parameters can be excluded, because the deviations compared to our derived Grüneisen parameters is negligible (see supplementary). In this way, the chosen model is similar to Eq. 2, while considering only the 3-phonon process (decay into two phonons), i.e. $\Delta_4 = 0$. This results in a linear dependence and was sufficient to describe the observed experiment data. To account for other linear processes in Δ_3, we rename it to $\Delta_{ac\text{-}ph}$. This now represents all anharmonic acoustic-phonon contributions. The lattice expansion contribution is included with the respective Grüneisen parameter. The ω_i values are chosen, as before for the optical phonons, as approximately the half of the respective acoustic phonon energy.

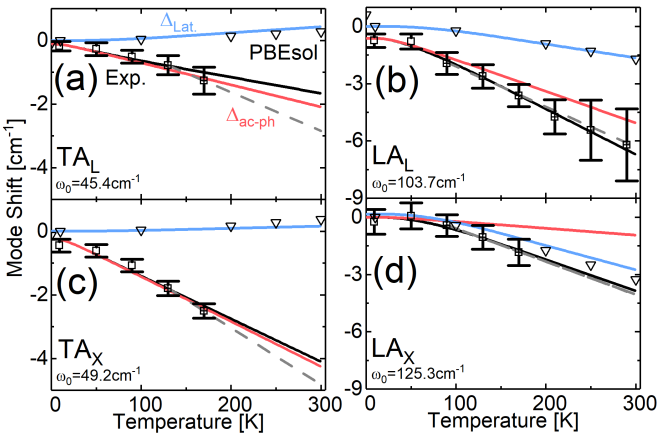

FIG. 5. Temperature dependent Raman shift of the second-order Raman scattering derived TA and LA phonons at the L- and X-point. The model for mode renormalization of optical phonons (black solid line, Eq. 2) was applied to fit the data points by only considering a lattice expansion contributions (blue solid lines) and a acoustic-phonon-like process (red solid lines). PBEsol predictions of mode shifts are as well indicated (black open triangles). The data points used for linear extrapolation (grey dashed lines) are indicated (black crossed-squares).

TABLE IV. Fit parameters (Eq. 2) of acoustic phonons energetic temperature dependence. ω_0 is the unperturbed phonon energy, ω_i the phonon energy of 3-phonon process like contribution and Δ_3 the zero temperature renormalization constant.

Mode	ω_0	ω_i	$\Delta_{ac\text{-}ph}$
TA_L	45.4	23	-0.11
TA_X	49.2	25	-0.25
LA_L	103.7	52	-0.63
LA_X	125.3	62	-0.16

The model is shown as well in Fig. 5(a-d). The respective parts of lattice expansion (blue) and the contributions from the acoustic-phonon process (red) are shown. The PBEsol prediction of the mode shift is also indicated (black triangles), which coincides well with the predicted lattice contribution. A linear extrapolation of the experimental data (dashed grey lines) shows negligible deviations compared to the model, especially for the LA phonons (i.e. $\lesssim 1 cm^{-1}$). This validates the extrapolated RT values for phonon energies of the TA_L, TA_X and LA_X modes. An extrapolation of the LA_X mode data points at higher temperatures can be done using the B_1 feature and the linear extrapolation of the A_3 feature. This agrees with the linear model up to RT. The unperturbed phonon energies are indicated by ω_0 and the listed in Tab. IV.

The validity of the model is indicated by a linear extrapolation, as shown in Fig. 5 (dashed grey line). Compared to the model fit, the linear extrapolation is almost identical for the LA phonons, while slight deviations are observed for the TA phonons (deviation at RT $\lesssim 1 cm^{-1}$). The model describes the experimentally observed behaviour quite well.

Only the TA modes show slight deviations at low temperatures. This could be linked to possible 3-phonon decay channels, which exist for the LA phonon (LA→TA+TA) but not for TA phonons [47]. For the TA phonons, only elastic interactions with thermal phonons can be expected [66]. The lattice contribution is negative for the TA mode, as observed for other zincblende semiconductors and is a consequence of the negative Grüneisen parameter [23, 63]. Its effect is quite small compared to the acoustic-phonon contribution and almost negligible for the TA_X mode. The mode shifts for the TA and LA modes at both critical points are comparable in magnitude. The lattice contribution plays a significant role for the LA modes, whereby it dominates for the LA_X mode.

The relative deviations by the calculated lattice contribution and the quasi-harmonic contribution from the PBEsol calculations are significant smaller for the longitudinal phonons than for the transversal phonons. The same trend is observed for the optical phonons and may be related to the transversal characteristics of the respective phonon modes. However, the absolute deviations are negligible and hence the lattice contribution is quite well resembled by the PBEsol theory.

The extrapolated and observed Raman shifts of the acoustic phonon modes at RT are in agreement with the results of the neutron scattering measurements from Hennion *et al.* [21] (Tab. II, Fig. 5(a)), except for the TA_L mode. We predict value of 43 cm^{-1} at RT, which is significant larger than 34 cm^{-1} [21] or 32 cm^{-1} [27]. For the neutron scattering measurements, this deviation is slightly larger than the error bars. We also note the significant overestimation of the LO phonon energy from neutron scattering compared to Raman spectroscopy measurements [69].

The TA mode positions and shifts can be supported by two different facts. Firstly, by comparing the linear extrapolation with inelastic neutron scattering measurements of CuI [63] (see supplementary). In this reference, a peak structure is observed at about 40 cm^{-1}, which we associate with the TA modes at L- and X-point. Secondly, by considering the temperature dependence of the phonons for the halide group semiconductor CuBr. The relative shifts of the TA phonons for CuBr are matching quite well to the observed relative shifts of the TA phonons of CuI [70].

The LA mode positions and shifts agree well for the L-point, while for the X-point some deviations are observed. The $[LO\text{-}LA]_L$ difference mode observed at 43cm^{-1}(Ref. [71]) as well as the relative shifts for the CuBr [70] support the LA_L assignment. Our observed relative shift for the LA_X mode is only 4% and hence lower than the relative shift of CuBr's LA_X mode with 14% [70]. The strong background signal at the B structure may reason an underestimation of the LA_X mode shift.

These results are summed up in Fig. 6 and validate the observed temperature trend of both TA phonons and the LA_L phonons. Especially at elevated temperatures the linear trend is observed for all acoustic phonons up to at RT. A model including lattice expansion and acoustic phonon processes could be used to describe this behavior. This seems to be valid at least up to RT and possibly as well above [63].

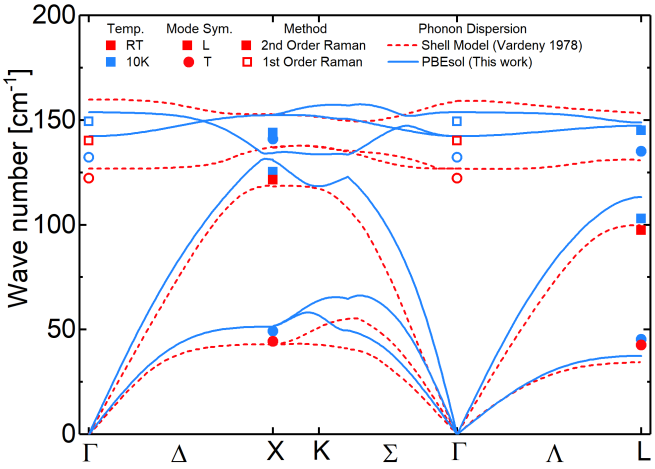

FIG. 6. Phonon dispersion along high symmetry directions from the shell model [55] (red dashed line, T = RT) and our PBEsol results (blue line, T = 10 K). Our experimental data from first- and second-order Raman scattering (open and full symbols). Red colors indicates RT and blue colors indicate a temperature of 10 K. Longitudinal modes are indicated by squares and transversal ones with circles. Note the significant deviations between Raman data and neutron scattering data (red dashed lines) for the TA_L and LO_Γ modes.

IV. SUMMARY

We observed second-order Raman scattering spectra on bulk CuI crystals, aside of the fundamental TO and LO modes. In total, 19 second-order Raman features were observed. By using DFT-based calculated 2-phonon density of states, the measured spectral shape was well reproduced. This way each feature was assigned to a two-phonon mode, which allowed to derive the energy of acoustic phonons by Raman spectroscopy. The temperature dependence of all phonons was analyzed as well.

The width and shift of optical zone-center phonons were characterized by considering quasi-harmonic lattice expansion and anharmonic phonon-phonon processes. Here the lattice expansion as well as 3- and 4-phonon processes play an important role. For acoustic phonons, this model was adapted and indicated a negligible lattice expansion for transversal acoustic phonons. For longitudinal acoustic phonons, the lattice expansion is of minor importance for modes at the L-point and dominating at the X-point. To quantify the results, the mode shift with temperature was calculated by DFT for all phonons. This shift is in accordance with the predicted lattice expansion. This can be explained with the quasi-harmonic nature of the lattice expansion approximation. For the acoustic phonons, the non-lattice-expansion related shift, indicates linear trend at elevated temperatures. Possible phonon-phonon processes are the 3-phonon decay or the elastic thermal phonon scattering. The observed acoustic phonon energies and shifts in CuI are in general in consistent with relative shifts observed for CuBr and also with neutron scattering data from literature.

V. ACKNOWLEDGMENT

We thank Evgeny Krüger for discussion and Lukas Trefflich as well as Gabriele Benndorf (both from the University of Leipzig) for technical support. We gratefully acknowledge funding from the Deutsche Forschungsgemeinschaft (DFG, German Research Foundation) through FOR 2857 - 403159832. Furthermore we acknowledge the Leibniz Supercomputing Center for granting computational resources (Project No. pn68le). R.H. acknowledges the Leipzig School of Natural Sciences BuildMoNa.

[1] G. Hautier, A. Miglio, G. Ceder, G.-M. Rignanese, and X. Gonze, *Identification and design principles of low hole effective mass p-type transparent conducting oxides,* Nature communications **4**, 2292 (2013).

[2] M. Grundmann, F.-L. Schein, M. Lorenz, T. Böntgen, J. Lenzner, and H. von Wenckstern, *Cuprous iodide: A p-type transparent semiconductor, history, and novel applications,* physica status solidi (a) **210**, 1671 (2013).

[3] D. Chen, Y. Wang, Z. Lin, J. Huang, X. Chen, D. Pan, and F. Huang, *Growth Strategy and Physical Properties of the High Mobility P-Type CuI Crystal,* Crystal Growth & Design **10**, 2057 (2010).

[4] C. Yang, D. Souchay, M. Kneiß, M. Bogner, H. M. Wei, M. Lorenz, O. Oeckler, G. Benstetter, Y. Q. Fu, and M. Grundmann, *Transparent flexible thermoelectric material based on non-toxic earth-abundant p-type copper iodide thin film,* Nature communications **8**, 16076 (2017).

[5] W. Lin, W. Wu, Q. Xie, Z. Liu, K. Qiu, L. Cai, Z. Yao, L. Meng, B. Ai, Z. Liang, and H. Shen, *Conductive Cuprous Iodide Hole-Selective Contacts with Thermal and Ambient Stability for Silicon Solar Cells,* ACS applied materials & interfaces **10**, 43699 (2018).

[6] A. Liu, H. Zhu, W.-T. Park, S.-J. Kim, H. Kim, M.-G. Kim, and Y.-Y. Noh, *High-performance p-channel transistors with transparent Zn doped-CuI,* Nature communications **11**, 4309 (2020).

[7] S.-D. Baek, D.-K. Kwon, Y. C. Kim, and J.-M. Myoung, *Violet Light-Emitting Diodes Based on p-CuI Thin Film/n-MgZnO Quantum Dot Heterojunction,* ACS applied materials & interfaces **12**, 6037 (2020).

[8] S. Koyasu, N. Umezawa, J. D. Baniecki, A. Yamaguchi, and M. Miyauchi, *Growth of Large Single Crystals of Copper Iodide by a Temperature Difference Method Using Feed Crystal Under Ambient Pressure,* Crystal Growth & Design **18**, 6748 (2018).

[9] P. Storm, M. S. Bar, G. Benndorf, S. Selle, C. Yang, H. von Wenckstern, M. Grundmann, and M. Lorenz, *High mobility, highly transparent, smooth, p-type CuI thin films grown by pulsed laser deposition,* APL Materials **8**, 091115 (2020).

[10] M. Wang, H. Wei, Y. Wu, C. Yang, P. Han, F. Juan, Y. Chen, F. Xu, and B. Cao, *Highly transparent and conductive γ-CuI films grown by simply dipping copper films into iodine solution,* Physica B: Condensed Matter **573**, 45 (2019).

[11] M. Wille, E. Krüger, S. Blaurock, V. Zviagin, R. Deichsel, G. Benndorf, L. Trefflich, V. Gottschalch, H. Krautscheid, R. Schmidt-Grund, and M. Grundmann, *Lasing in cuprous iodide microwires,* Applied Physics Letters **111**, 031105 (2017).

[12] M. Nakamura, S. Inagaki, Y. Okamura, M. Ogino, Y. Takahashi, K. Adachi, D. Hashizume, Y. Tokura, and M. Kawasaki, *Band structures in orientation-controlled CuI thin films under epitaxial strain,* Physical Review B **106**, 125307 (2022).

[13] E. Mallet, F. Réveret, P. Disseix, T. V. Shubina, and J. Leymarie, *Influence of excitonic oscillator strengths on the optical properties of GaN and ZnO,* Physical Review B **90**, 045204 (2014).

[14] S. Inagaki, M. Nakamura, Y. Okamura, M. Ogino, Y. Takahashi, L. C. Peng, X. Z. Yu, Y. Tokura, and M. Kawasaki, *Heteroepitaxial growth of wide bandgap cuprous iodide films exhibiting clear free-exciton emission,* Applied Physics Letters **118**, 012103 (2021).

[15] E. Krüger, M. S. Bar, S. Blaurock, L. Trefflich, R. Hildebrandt, A. Müller, O. Herrfurth, G. Benndorf, H. von Wenckstern, H. Krautscheid, M. Grundmann, and C. Sturm, *Dynamics of exciton–polariton emission in CuI,* APL Materials **9**, 121102 (2021).

[16] M. Xia, M. Gu, X. Liu, B. Liu, S. Huang, and C. Ni, *Luminescence characteristics of CuI film by iodine annealing,* Journal of Materials Science: Materials in Electronics **26**, 5092 (2015).

[17] G. Lin, F. Zhao, Y. Zhao, D. Zhang, L. Yang, X. Xue, X. Wang, C. Qu, Q. Li, and L. Zhang, *Luminescence Properties and Mechanisms of CuI Thin Films Fabricated by Vapor Iodization of Copper Films,* Materials **9**, 990 (2016).

[18] S. Jaschik, M. R. G. Marques, M. Seifert, C. Rödl, S. Botti, and M. A. L. Marques, *Stable Ordered Phases of Cuprous Iodide with Complexes of Copper Vacancies,* Chemistry of Materials **31**, 7877 (2019).

[19] Y. Li, J. Sun, and D. J. Singh, *Optical and electronic properties of doped p-type CuI: Explanation of transparent conductivity from first principles,* Phys. Rev. Mater. **2**, 035003 (2018).

[20] Z.-L. Xu, C. Yang, and Y.-N. Wu, *Temperature-dependent electronic structure of γ-phase CuI: first-principles insights,* Journal of Physics: Condensed Matter **34**, 134002 (2022).

[21] B. Hennion, F. Moussa, B. Prevot, C. Carabatos, and C. Schawb, *Normal Modes of Vibrations in CuI,* Physical Review Letters **28**, 964 (1972).

[22] J. N. Plendl, A. Hadni, J. Claudel, Y. Henninger, G. Morlot, P. Strimer, and L. C. Mansur, *Far infrared study of the copper halides at low temperatures,* Applied optics **5**, 397 (1966).

[23] J. Serrano, M. Cardona, T. M. Ritter, B. A. Weinstein, A. Rubio, and C. T. Lin, *Pressure and temperature dependence of the Raman phonons in isotopic γ-CuI,* Physical Review B **66**, 245202 (2002).

[24] H. He and Z. Zhang, *Decay mechanism of optical phonons in γ-CuI,* AIP Advances **9**, 055104 (2019).

[25] J. E. Potts, C. T. Walker, and I. R. and Nair, *Temperature Dependence of Second-Order Raman Scattering in Potassium and Rubidium Halides,* Physical Review B **8**, 2756 (1972).

[26] T. Fukumoto, K. Tabuchi, S. Nakashima, and A. Mituishi, *Temperature dependence of Raman linewidth and shift in CuI,* Optics Communications **10**, 78 (1974).

[27] O. Brafman, M. Cardona, and Z. and Vardeny, *Raman-scattering study of pressure-induced phase transitions in CuI,* Physical Review B **15**, 1081 (1976).

[28] T. Fukumoto, S. Nakashima, K. Tabuchi, and A. Mitsuishi, *Temperature Dependence of Raman Spectra of Cuprous Halides,* physica status solidi (b) **73**, 341 (1976).

[29] B. Prevot and M. Sieskind, *First and Second Order Raman Scattering in CuBr and CuI,* Phys. Status Solidi B **61**, 121

(1974).
[30] J. Zhou, H. D. Shin, K. Chen, B. Song, R. A. Duncan, Q. Xu, A. A. Maznev, K. A. Nelson, and G. Chen, *Direct observation of large electron-phonon interaction effect on phonon heat transport,* Nat. Commun. **11**, 6040 (2020).
[31] Z. Bai, D. He, S. Fu, Q. Miao, S. Liu, M. Huang, K. Zhao, Y. Wang, and X. Zhang, *Recent progress in electron–phonon interaction of two–dimensional materials,* Nano Select **3**, 1112 (2022).
[32] Z. Aksamija and U. Ravaioli, *Anharmonic decay of non-equilibrium intervalley phonons in silicon,* Journal of Physics: Conference Series **193**, 012033 (2009).
[33] T. Kirchartz, T. Markvart, U. Rau, and D. A. Egger, *Impact of Small Phonon Energies on the Charge-Carrier Lifetimes in Metal-Halide Perovskites,* The Journal of Physical Chemistry Letters **9**, 939 (2018).
[34] P. G. Klemens, *Anharmonic Decay of Optical Phonons,* Physical Review **148**, 845 (1966).
[35] D. Hardt and R. Bollig, *Darstellung von Schwermetallhalogeniden in wasserfreier Essigsäure,* Angew. Chem. **77**, 860 (1965).
[36] P. Gao, M. Gu, X. Liu, C.-F. Yang, Y.-Q. Zheng, and E.-w. Shi, *Large CuI crystal growth by evaporation technique and its growth mechanism,* CrystEngComm **15**, 2934 (2013).
[37] G. Kresse and J. Furthmüller, *Efficiency of ab-initio total energy calculations for metals and semiconductors using a plane-wave basis set,* Computational Materials Science **6**, 15 (1996).
[38] G. Kresse and D. Joubert, *From ultrasoft pseudopotentials to the projector augmented-wave method,* Physical review. B, Condensed matter **59**, 1758 (1999).
[39] Blöchl, *Projector augmented-wave method,* Physical Review B **50**, 17953 (1994).
[40] M. Seifert, M. Kawashima, C. Rödl, and S. Botti, *Layered CuI: a path to 2D p-type transparent conducting materials,* Journal of Materials Chemistry C **9**, 11284 (2021).
[41] M. Seifert, E. Krüger, M. S. Bar, S. Merker, H. von Wenckstern, H. Krautscheid, M. Grundmann, C. Sturm, and S. Botti, *Dielectric function of $CuBr_xI_{1-x}$ alloy thin films,* Physical Review Materials **6**, 124601 (2022).
[42] I. Pallikara, P. Kayastha, J. M. Skelton, and L. D. Whalley, *The physical significance of imaginary phonon modes in crystals,* Electronic Structure **4**, 033002 (2022).
[43] J. P. Perdew, A. Ruzsinszky, G. I. Csonka, O. A. Vydrov, G. E. Scuseria, L. A. Constantin, X. Zhou, and K. Burke, *Restoring the density-gradient expansion for exchange in solids and surfaces,* Physical Review Letters **100**, 136406 (2008).
[44] A. Togo, F. Oba, and I. Tanaka, *First-principles calculations of the ferroelastic transition between rutile-type and $CaCl_2$-type SiO_2 at high pressures,* Phys. Rev. B **78**, 134106 (2008).
[45] A. Togo and I. Tanaka, *First principles phonon calculations in materials science,* Scripta Materialia **108**, 1 (2015).
[46] R. P. Stoffel, C. Wessel, M.-W. Lumey, and R. Dronskowski, *Ab Initio Thermochemistry of Solid-State Materials,* Angewandte Chemie International Edition **49**, 5242 (2010).
[47] K. Okubo and S.-i. Tamura, *Two-phonon density of states and anharmonic decay of large-wave-vector LA phonons,* Physical Review B **28**, 4847 (1983).
[48] J. L. Birman, *Theory of Infrared and Raman Processes in Crystals: Selection Rules in Diamond and Zincblende,* Physical Review **131**, 1489 (1963).
[49] M. Cardona, G. Güntherodt, R. K. Chang, M. B. Long, and H. Vogt, *Light Scattering in Solids II: Basic Concepts and Instrumentation*, 1st ed. (Springer-Verlag Berlin Heidelberg, 1981).
[50] R. Loudon, *The Raman effect in crystals,* Advances in Physics **50**, 813 (2001).
[51] J. C. Irwin and J. LaCombe, *Second-order Raman spectrum of ZnSe,* ACS applied materials & interfaces **48**, 2499 (1970).
[52] J. Serrano, A. Cantarero, M. Cardona, N. Garro, R. Lauck, R. E. Tallman, T. M. Ritter, and B. A. Weinstein, *Raman scattering in β-ZnS,* Physical Review B **69**, 014301 (2004).
[53] N. Vagelatos, D. Wehe, and J. S. King, *Phonon dispersion and phonon densities of states for ZnS and ZnTe,* The Journal of Chemical Physics **60**, 3613 (1974).
[54] J. L. La Combe, *Raman studies of phonon dispersion in zincblende semiconductors.*, Dissertation, Simon Fraser University, Burnaby, Canada (1971).
[55] Z. Vardeny, G. Gilat, and D. and Moses, *Specific heats and lattice dynamics of cuprous halides,* Physical Review B **18**, 4487 (1978).
[56] F. A. Johnson and R. Loudon, *Critical-point analysis of the phonon spectra of diamond, silicon and germanium,* Proceedings of the Royal Society A **281**, 274 (1964).
[57] R. W. Keyes, *Trends in the Lattice "Combination Bands" of Zincblende–type Semiconductors,* The Journal of Chemical Physics **37**, 72 (1962).
[58] S. S. Mitra, *Phonon Assignments in ZnSe and GaSb and Some Regularities in the Phonon Frequencies of Zincblende-Type Semiconductors,* Physical Review **12**, 986 (1963).
[59] G. Petretto, S. Dwaraknath, H. P. C. Miranda, D. Winston, M. Giantomassi, M. J. van Setten, X. Gonze, K. A. Persson, G. Hautier, and G.-M. Rignanese, *High-throughput density-functional perturbation theory phonons for inorganic materials,* Scientific data **5**, 180065 (2018).
[60] W. H. Weber and R. Merlin, *Raman Scattering in Materials Science* (Springer-Verlag Berlin Heidelberg, 2000).
[61] M. Giehler, M. Ramsteiner, P. Waltereit, O. Brandt, K. H. Ploog, and H. Obloh, *Influence of heteroepitaxy on the width and frequency of the E2 (high)-phonon line in GaN studied by Raman spectroscopy,* Journal of Applied Physics **89**, 3634 (2001).
[62] M. Balkanski, R. F. Wallis, and E. Haro, *Anharmonic effects in light scattering due to optical phonons in silicon,* Physical Review B **28**, 1928 (1983).
[63] A. M. Gopakumar, M. K. Gupta, R. Mittal, S. Rols, and S. L. Chaplot, *Investigating anomalous thermal expansion of copper halides by inelastic neutron scattering and ab initio phonon calculations,* Physical Chemistry Chemical Physics **19**, 12107 (2017).
[64] J. N. Plendl and L. C. Mansur, *Anomalous thermal expansion with infrared spectroscopy,* Applied optics **11**, 1194 (1972).
[65] F. Knoop, T. A. R. Purcell, M. Scheffler, and C. Carbogno, Anharmonicity in Thermal Insulators: An Analysis from First Principles, (2023), arXiv:2209.12720.
[66] J. Kulda, A. Debernardi, M. Cardona, F. de Geuser, and E. E. Haller, *Self-energy of zone-boundary phonons in germanium: Ab initio calculations versus neutron spin-echo measurements,* Physical Review B **69**, 045209 (2004).
[67] F. Li, J. Shen, S. R. Parnell, A. N. Thaler, M. Matsuda, T. Keller, O. Delaire, R. Pynn, and J. A. Fernandez-Baca, *High-resolution phonon energy shift measurements with the inelastic neutron spin echo technique,* Journal of Applied Crystallography **52**, 755 (2019).
[68] M. Kempa, P. Ondrejkovic, P. Bourges, J. Ollivier, S. Rols, J. Kulda, S. Margueron, and J. Hlinka, *The temperature dependence of the phononic band gap of NaI,* Journal of Physics: Condensed Matter **25**, 055403 (2013).

[69] J. E. Potts, R. C. Hanson, and Walker, C. T.,Schwab,C., *Raman Scattering from CuBr and CuI,* Solid State Communications **13**, 389 (1973).

[70] S. Hoshino, Y. Fujii, J. Harada, and J. D. Axe, *Neutron Scattering Study of Lattice Dynamics in CuBr Part I. Phonon Dispersion Relations,* Journal of the Physcial Society of Japan **41**, 965 (1976).

[71] G. Livescu and O. Brafman, *Raman study of the mixed crystals $Cu_xAg_{1-x}I$,* Journal of Physics C: Solid State Physics **19**, 2663 (1986).

Supplemental Material: Temperature dependent second-order Raman scattering in CuI

R. Hildebrandt,[1,*] M. Seifert,[2] J. George,[3,2] S. Blaurock,[4] S. Botti,[2] H. Krautscheid,[4] M. Grundmann,[1] and C. Sturm[1]

[1]*Universität Leipzig, Felix Bloch Institute for Solid State Physics, Semiconductor Physics Group, Linnéstraße 5, 04103 Leipzig*

[2]*Friedrich-Schiller-Universität Jena, Institute of Condensed Matter Theory and Optics, Max-Wien-Platz 1, 07743 Jena*

[3]*Federal Institute for Materials Research and Testing Department Materials Chemistry, Unter den Eichen 87, 12205 Berlin*

[4]*Univerität Leipzig, Institute for Inorganic Chemistry, Johannisallee 29, 04103 Leipzig*

(Dated: May 25, 2023)

I. THERMAL EXPANSION COEFFICIENT

The shift of the phonon mode is determined by the Grüneisen parameters and the coefficient of thermal expansion (CTE). The used CTE is shown in Fig. S1 and was derived by using the bulk lattice constant measured in Ref. 1. This CTE is in accordance with other results [2, 3].

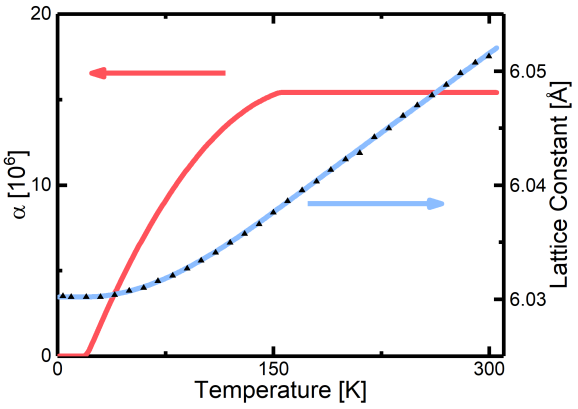

FIG. S1. The experimental data represents the lattice constants (triangles) and the data is taken from Ref. 1. The respective used lattice constant is shown (blue line), which yields the derived coefficient of thermal expansion (red line).

II. TA PHONON TEMPERATURE DEPENDENCE

The extrapolation of the TA modes to higher temperatures and comparison with results from neutron scattering from Ref. [2] is shown in Fig. S2. The extrapolation supports the identified temperature dependence of TA phonons.

III. ADDITIONAL INFORMATION ABOUT PHONON CALCULATION

Important quantities for the phonon calculations are the size of the supercell as well as the corresponding **k**-point grid for the computation of the forces as part of the finite displacement method. To discuss the influence of those regarding the results shown in the manuscript the convergence of certain modes at certain high-symmetry points of the Brillouin zone are shown in Fig. S3. These specific modes are chosen, since they were also discussed in the main manuscript. It is shown, that both increasing the supercell size as well as the density of the **k**-point grid causes differences smaller than

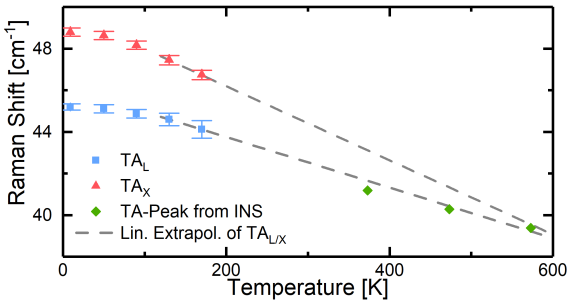

FIG. S2. Second-order Raman scattering determined phonon energies of both TA modes and the TA peak positions at elevated temperatures from the inelastic neutron scattering [2]. The linear extrapolation of our determined TA phonon energies agrees well with their TA peak positions.

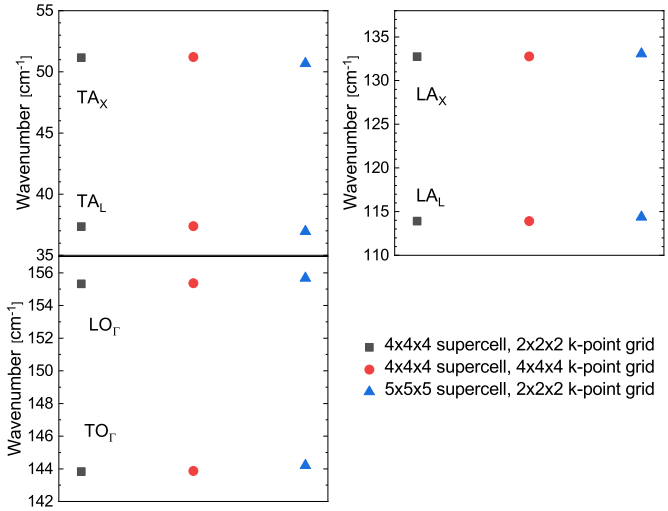

FIG. S3. Influence of the supercell size and the corresponding **k**-point grid on the wavenumbers of exemplary phonon modes at certain high-symmetry point in the Brillouin zone. Calculated at T=0 K.

* ron.hildebrandt@uni-leipzig.de

1 %. To compute temperature-dependent phonon modes, we

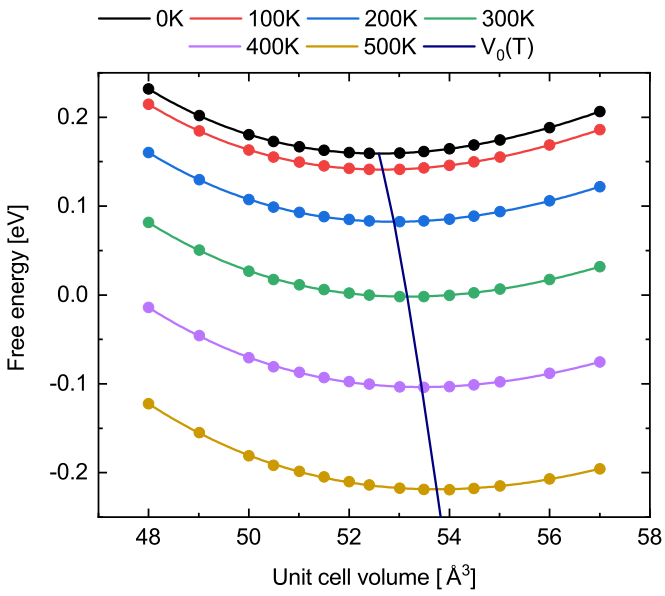

FIG. S4. Determination of the temperature-dependent volume via fitting a Vinet equation of states.

applied the quasi-harmonic approximation to obtain the free energy at different volumes. Then the temperature-dependent volume of the unit cell was obtained by fitting a Vinet equation of states to the corresponding temperature curves. These steps were performed using phonopy [4, 5]. In Fig. S4 those curves are exemplarily shown for some temperatures as well as the development of the equilibrium volume.

IV. GRÜNEISEN PARAMETER COMPARISON

In the manuscript, we mentioned negligible deviations of our calculated Grüneisen parameter γ at specific high-symmetry points to the literature values. This is displayed via the Grüneisen band structure of CuI in Fig. S5 including the respective literature values.

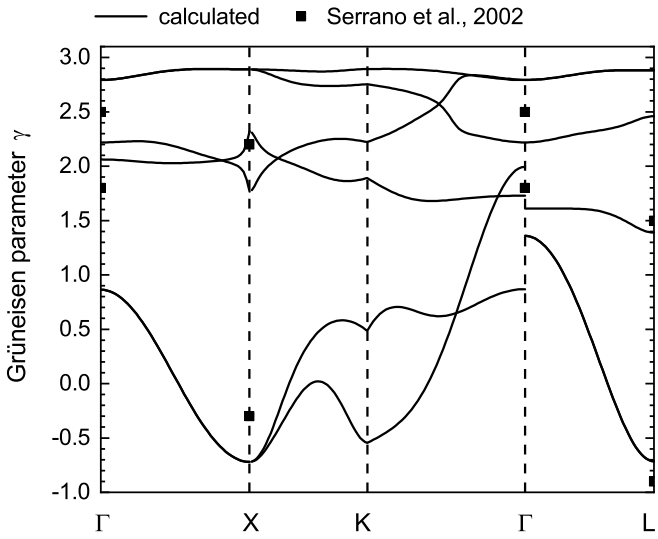

FIG. S5. Our calculated Grüneisen band structure of CuI. Square symbols are Grüneisen parameters from Ref. [6] used to calculate $\Delta_{\text{Lat.}}$: $\gamma(\text{TO}_\Gamma) = 1.8$, $\gamma(\text{LO}_\Gamma) = 2.5$, $\gamma(\text{TA}_\text{L}) = -0.9$, $\gamma(\text{TA}_\text{X}) = -0.3$, $\gamma(\text{LA}_\text{L}) = 1.5$ and $\gamma(\text{LA}_\text{X}) = 2.2$.

[1] M. Nakamura, S. Inagaki, Y. Okamura, M. Ogino, Y. Takahashi, K. Adachi, D. Hashizume, Y. Tokura, and M. Kawasaki, *Band structures in orientation-controlled cui thin films under epitaxial strain*, Band structures in orientation-controlled cui thin films under epitaxial strain, Physical Review B **106**, 125307 (2022).

[2] A. M. Gopakumar, M. K. Gupta, R. Mittal, S. Rols, and S. L. Chaplot, *Investigating anomalous thermal expansion of copper halides by inelastic neutron scattering and ab initio phonon calculations*, Investigating anomalous thermal expansion of copper halides by inelastic neutron scattering and ab initio phonon calculations, Physical Chemistry Chemical Physics **19**, 12107 (2017).

[3] J. N. Plendl and L. C. Mansur, *Anomalous thermal expansion with infrared spectroscopy*, Anomalous thermal expansion with infrared spectroscopy, Applied optics **11**, 1194 (1972).

[4] A. Togo, F. Oba, and I. Tanaka, *First-principles calculations of the ferroelastic transition between rutile-type and cacl$_2$-type sio$_2$ at high pressures*, First-principles calculations of the ferroelastic transition between rutile-type and cacl$_2$-type sio$_2$ at high pressures, Phys. Rev. B **78**, 134106 (2008).

[5] A. Togo and I. Tanaka, *First principles phonon calculations in materials science*, First principles phonon calculations in materials science, Scripta Materialia **108**, 1 (2015).

[6] J. Serrano, M. Cardona, T. M. Ritter, B. A. Weinstein, A. Rubio, and C. T. Lin, *Pressure and temperature dependence of the raman phonons in isotopic γ-cui*, Pressure and temperature dependence of the raman phonons in isotopic γ-cui, Physical Review B **66**, 245202 (2002).